The Astrophysical Journal, 902:153 (12pp), 2020 October 20 https://doi.org/10.3847/1538-4357/abb3c7

Imagery and UV Spectroscopy of the LMC Supernova Remnant N103B Using HST

William P. Blair[1], Parviz Ghavamian[2], John C. Raymond[3], Brian J. Williams[4], Ravi Sankrit[5], Knox S. Long[5,6], P. Frank Winkler[7], Norbert Pirzkal[5], and Ivo R. Seitenzahl[8]

[1] The Henry A. Rowland Department of Physics and Astronomy, Johns Hopkins University, 3400 N. Charles Street, Baltimore, MD 21218, USA; wblair@jhu.edu
[2] Towson University, Towson, MD 21252, USA; pghavamian@towson.edu
[3] Harvard-Smithsonian Center for Astrophysics, 60 Garden Street, Cambridge, MA 02138, USA; raymond@cfa.harvard.edu
[4] NASA Goddard Spaceflight Center, Greenbelt, MD 20771, USA; brian.j.williams@nasa.gov
[5] Space Telescope Science Institute, 3700 San Martin Drive, Baltimore, MD 21218, USA; rsankrit@stsci.edu, npirzkal@stsci.edu
[6] Eureka Scientific, Inc. 2452 Delmer Street, Suite 100, Oakland, CA 94602-3017; long@stsci.edu
[7] Department of Physics, Middlebury College, Middlebury, VT 05753, USA; winkler@middlebury.edu
[8] School of Science, University of New South Wales, Northcott Drive, Canberra, ACT, 2600, Australia; i.seitenzahl@adfa.edu.au
Received 2020 July 8; revised 2020 August 25; accepted 2020 August 27; published 2020 October 23

Abstract

We present Hubble Space Telescope (HST)/Wide Field Camera 3 multiband imagery of N103B, which is the remnant of a SN Ia in the Large Magellanic Cloud, as well as HST/Cosmic Origins Spectrograph (COS) ultraviolet spectroscopy of the brightest radiatively shocked region. The images show a wide range of morphology and relative emission-line intensities, from smooth Balmer-line dominated collisionless shocks that are due to the primary blast wave to clumpy radiative shock filaments that are due to secondary shocks in density enhancements. The COS data show strong FUV line emissions, despite a moderately high extinction along this line of sight. We use the COS data with previous optical spectra to constrain the shock conditions, we refine the abundance analysis, and we find abundances that are typical of the local interstellar medium within the uncertainties. Under an assumption that the material being shocked was shed from the pre-supernova system, this finding places constraints on any significant enrichment in that material, and thus on the non-degenerate star in what was presumably a single-degenerate SN Ia.

Unified Astronomy Thesaurus concepts: Supernova remnants (1667); Nebulae (1095); Emission nebulae (461); Shocks (2086); Type Ia supernovae (1728)

1. Introduction

Type Ia supernovae (SNe) are now widely understood to arise from the thermonuclear destruction of a white dwarf star, but the progenitor systems and exact trigger mechanisms for the explosion are still unclear (Heringer et al. 2017; Livio & Mazzali 2018). SNe Ia are believed to be caused either by coalescence of two white dwarf stars (the so-called double-degenerate scenario: Iben & Tutukov 1984; Webbink 1984; Livio & Riess 2003) or by an alternative mechanism, such as runaway nuclear burning of one type or another on a white dwarf star caused by accretion from a non-degenerate companion star (single-degenerate scenario: Whelan & Iben 1973; Nomoto 1982a, 1982b; Nomoto & Leung 2018). There are a number of additional theoretical possibilities within these two general pathways, such as common envelope scenarios and core-degenerate models (Kashi & Soker 2011; Ilkov & Soker 2012; Wang & Han 2012; Meng & Podsiadlowski 2017; Wang et al. 2017). These scenarios have ramifications for the progenitor system, as reviewed recently by Ruiz-Lapuente (2019). Many authors have suggested that the double-degenerate pathway dominates (see Totani et al. 2008; Liu et al. 2018) but there remain intriguing counterexamples that seem to point toward some version of a single-degenerate scenario for at least some SNe Ia (Blair et al. 2007; Reynolds et al. 2007; Williams et al. 2011, 2012), including N103B—the subject of this paper (Williams et al. 2014; Sano et al. 2018).

Conclusive evidence in favor of the single-degenerate mechanism has been difficult to find. One of the most promising methods used so far is to search for evidence of interaction between the supernova remnant and a dense circumstellar wind of the type expected to be generated prior to the explosion by the donor star (Hachisu et al. 1996; Badenes et al. 2007; Chiotellis et al. 2012).[9] Kepler's supernova remnant is a promising candidate, wherein the Balmer-dominated shocks are driving secondary shocks into dense clumps, which produces radiative shocks (Blair et al. 1991; Sankrit et al. 2016). There is evidence from Spitzer observations for a non-standard silicate-rich dust component in the shocked material (Williams et al. 2012), presumably indicating an origin in the mass lost from the stellar wind of the non-degenerate donor star (Ossenkopf et al. 1992; Henning 2010). Since Kepler's SNR is well off the plane of the Galaxy, a clumpy, dense surrounding interstellar medium (ISM) is not expected. This strengthens the conclusion that the shocked material is circumstellar and not interstellar in origin.

A second SNR has recently been identified as a candidate for a single-degenerate Type Ia: N103B (SNR 0509−68.7) in the Large Magellanic Cloud (Williams et al. 2014). X-ray analyses of N103B (Hughes et al. 1995; Lewis et al. 2003; Lopez et al. 2011; Yamaguchi et al. 2014) indicate an Fe/O abundance and morphology consistent with a Type Ia explosion. This conclusion is confirmed by an actual spectrum of the SN derived from a light echo (A. Rest 2020, private communication). In optical images, the SNR exhibits a prominent collection of compact, bright knots emitting in Hα, [S II], and [O III](Williams et al. 2014; Li et al. 2017) embedded within a smooth partial shell filaments emitting only H Balmer-line emission. Li et al. (2017) also identify a potential companion star that was left behind after

[9] However, see Levanon et al. (2015) and Levanon & Soker (2019) for a discussion of possible circumstellar material from certain double-degenerate models.

the explosion, which, if true, would strengthen the case for a single-degenerate explosion.[10]

Spitzer observations by Williams et al. (2014) showed a very bright 24 μm emission that arises from warm dust heated by the forward shock, seen in Hα and with morphology reminiscent of a bow shock open to the east. This structure is consistent with the shock sweeping into a wind from the progenitor system within an overall density gradient, which is similar to the structure seen in Kepler's SNR. The derived densities in both Kepler and N103B are also nearly identical, $\sim$40–45 cm^{-3}, which would be high for normal ISM ($\leqslant$1 cm^{-3}). The Spitzer IRS spectrum of N103B is essentially identical to that of Kepler, with a peculiar "18 μm" silicate bump offset to $\sim$17.2 μm and a warm dust continuum ($\sim$115–130 K; Williams et al. 2014). All of these similarities to Kepler's SNR imply a similar origin for the material being encountered by the shock in N103B (i.e., circumstellar material from the progenitor system).

The size of this SNR ($\sim$30″ across, or $D = 7.2$ pc at the LMC distance of 50 kpc) indicates a SNR larger than Kepler ($D = 4.9$ pc assuming a distance of 5 kpc) but similar in size to Tycho's SNR (SN 1572). The light echoes from N103B mentioned earlier place its age at approximately 860 yr (Rest et al. 2005), which would make N103B nearly twice as old as Tycho and Kepler. However, a younger age is possible according to Rest et al. (2005), depending on the characteristics of the dust screen responsible for the light echo. Ghavamian et al. (2017) estimate a Sedov age of 685 $\pm$ 20 yr, while an X-ray expansion measurement by Williams et al. (2018) also implies an age less than 850 yr. Since the distance (and diameter) are known, one can calculate a mean expansion velocity for an assumed age. Using the age range 685–860 yr, the mean expansion velocity must have been in the range 5009–3986 km s^{-1}, respectively. The current average observed shock velocity reported by Ghavamian et al. (2017) is 2070 $\pm$ 60 km s^{-1}, which is well below this range and indicates that a significant deceleration of the primary shock has occurred.

Recently, Li et al. (2017) have presented both narrowband Hα and broadband imagery of N103B taken with the Wide Field Camera 3 (WFC3) instrument on Hubble Space Telescope (HST), as well as ground-based echelle longslit spectroscopy. The HST images indicated that the filaments forming the outer shell of N103B exhibit the smooth, delicate morphology characteristic of Balmer-dominated shocks. Their spectra confirm broad Balmer emission from these filaments, but their observations were not sufficient to reveal the full extent of the broad component velocities.

Ghavamian et al. (2017) presented integral field observations of N103B acquired with the Wide Field Imaging Spectrograph (WiFeS; Dopita et al. 2007, 2010) on the 2.3 m telescope of the Australian National University. These observations covered the spectral range 3500–7000 Å and allowed measurement of the full extent of the broad Hα line both in the interior and along the southern and northern limbs of N103B. Coronal [Fe XIV] λ5303 emission from the nonradiative shocks was detected in MUSE observations by Seitenzahl et al. (2019). Dopita et al. (2019) presented an in-depth analysis of spectra from a number of LMC SNRs, including the brightest radiative knot near the center of N103B. They performed a detailed assessment of elemental abundances and found that the abundances of heavy elements in these SNRs are consistent with standard LMC abundances as derived from other sources. Li et al. (2017) also showed high-resolution spectra of this same bright knot in N103B, which revealed highly redshifted ($\sim$370 km s^{-1}), somewhat broadened ($\sim$190 km s^{-1}) Hα emission.

Sano et al. (2018) investigated the molecular gas in the direction of N103B using CO observations with ATCA and the Atacama Submillimeter Telescope Experiment, covering both moderate and high resolutions. Interestingly, molecular clouds are seen directly adjacent to N103B, but they are seen in the south and southeast and not in the west where the optical nonradiative shocks are brightest. Hence, while there may be some interaction with molecular gas, it does not yet appear to be in full force; otherwise, the optical and X-ray shocks would be brighter in the south and southeast.

Here, we present additional HST WFC3 narrowband imagery of N103B in the light of selected optical and near-IR emission lines. We also present a far-ultraviolet Cosmic Origins Spectrograph (COS) spectrum of the central radiatively shocked knot in N103B (the same cloud targeted by Dopita et al. 2019 and Li et al. 2017). The COS spectrum provides improved abundance information on elements such as carbon and silicon that are poorly constrained by optical data alone and can be affected by shock processing of dust grains. We describe these observations in the next section, we present the modeling and abundance determinations in Section 3, and we then discuss the results in the context of comparison with Kepler's SNR in Section 4. We summarize our findings in Section 5.

Table 1
HST Observations of N103B

Instrument	Filt/Gr	Dithers	Total Exp (s)
WFC3-UVIS	F657N	4	2979
WFC3-UVIS	F673N	4	1982
WFC3-UVIS	F502N	4	2051
WFC3-UVIS	F547M	4	782
WFC3-IR	F164N	4	2012
WFC3-IR	F160W	3	339
COS	G140L	(4)[a]	2639

Note.
[a] FP-POS positions.

2. Observations

The HST data discussed and used below are available from the Mikulski Archive for Space Telescopes (MAST) and can be accessed at 10.17909/t9-bddp-1b43.

2.1. HST Imaging

The WFC3 data were obtained on 2017 January 3 under program ID GO-14359, which was part of a joint Chandra-HST program (B. J. Williams, PI); both the UVIS and IR cameras were used, as shown in Table 1. The UVIS data included the filters F657N (Hα), F673N ([S II]), F502N ([O III]) and F547M (continuum), and the IR camera data included F164N ([Fe II]) and F160W (continuum), thus sampling the bright emissions expected from radiative shocks, with Hα also sampling the fainter nonradiative shocks identified by Li et al. (2017) and Ghavamian et al. (2017), which are dominated by hydrogen

[10] No confirmation of this candidate has to our knowledge been made, although Li et al. (2019) have recently identified possible companions in two other LMC SNIa remnants using a kinematic criterion.

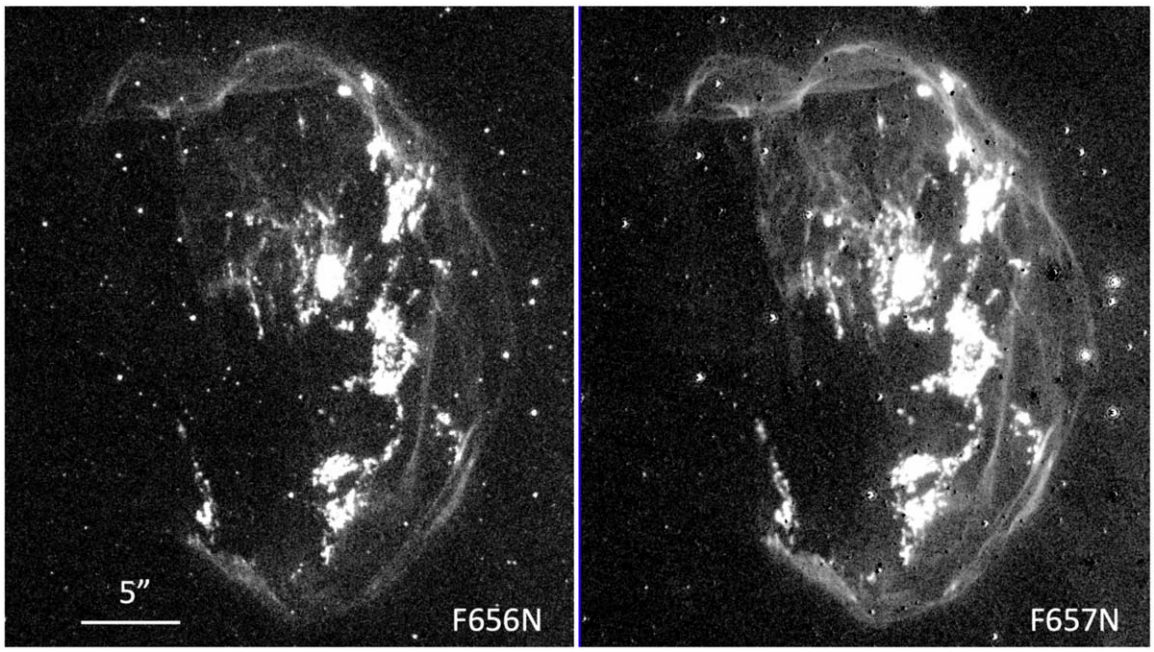

Figure 1. Comparison figure showing aligned WFC3 images of N103B in the narrow F656N filter (program 13282) and our wider F657N filter image. Log scaling of the display is used to bring out the details in the faintest emission. The broader F657N filter captures significantly more detail in the faint, smooth filaments, which are attributed to nonradiative emission from the primary shock front. Both images have had a continuum image subtracted to remove stars to first order, but a number of stellar residuals remain. Close inspection of stellar-appearing features can reveal whether the feature is a real emission knot or a stellar residual from imperfect subtraction. In this and other images, north is up and east to the left.

Balmer emission. The continuum bands were nominally for identifying stars and, as needed, we subtracted them to provide a cleaner look at the SNR emission. The observations obtained in each filter were dithered to permit removal of artifacts from the data and (for UVIS) to cover the chip gap, and the appropriate FLASH parameter was set for UVIS to reduce the effects of charge transfer inefficiency. The combined images in each filter that were produced by the data processing pipeline were sufficient for the needs of this program.

The F547M filter was selected to obtain a continuum band reasonably close to the bandpass of the other optical filters to identify stars. However, N103B exhibits a number of faint (and yet unusually strong for typical SNR emission) [Fe II] emission lines that lie within the bandpass of F547M (see Dopita et al. 2019, Table 8),[11] causing the bright radiative filaments to be visible at a low level within the F547M image (see Figure 2). For display purposes, we scale and subtract the F547M data from the emission-line frames; however, since the stellar density is not severe, flux information has been derived directly from the original emission-line data frames.

In this program the wider F657N filter (FWHM = 121 Å) was used instead of the F656N filter (FWHM = 18 Å) used by (Li et al. 2017, program GO-13282, Y.-H. Chu, PI) to make sure that the full range of Hα emission was detected, especially given the $\sim$250 km s^{-1} redshift of the LMC itself. Our "Hα" image thus contains emissions from both [N II] $\lambda\lambda$6548, 6583 and Hα for the radiative filaments, which can be identified by their clumpy, structured morphology. Even so, [N II] is fairly weak compared with Hα in the LMC due to relatively low N abundance, so Hα is expected to dominate the F657N image, even for the radiative filaments. We have reprocessed and astrometrically aligned the F656N dataset to our new data (registration within 0.2 pixels), and a comparison is shown in Figure 1. This figure is scaled to show the faint emission to best effect, and the improved signal-to-noise for the faint Balmer filaments is apparent. Details of the structure of faint Balmer filaments can be clearly seen in the right-hand panel of Figure 1. We note that both images in Figure 1 have been continuum subtracted using the F547M image. Close inspection, especially for the F657N frame, makes it clear that there are a number of very small angular size knots of emission that are real, while stellar residuals can be identified due to a very small offset in alignment between F547M and the emission-line filters.

The WFC3 IR camera was used to observe [Fe II] λ1.644 μm using the F164N filter, and F160W H-band was used for continuum. The emission line of interest is actually within the passband of the continuum filter, so some SNR emission is visible in the raw F160W data. However, the star density is again not severe and [Fe II] fluxes can be extracted directly from the F164N image.

We show the resulting images in Figures 2 and 3. Figure 2 shows a set of 40″ regions centered on N103B and indicates the full extent of optical/NIR emission. The color panel is made with the three optical emission lines, after subtracting a scaled version of the F547M image. Again, for display purposes, no correction for the faint filament emission visible in F547M was made. The faint, smooth, filament arcs visible only in Hα (red) are the fast nonradiative shocks described earlier showing the position of the primary shock front; their full extent and morphology are best seen in the right-hand panel of Figure 1. The filaments that show as yellow or white in the color panel of Figure 2 are bright in Hα, [S II], and [O III], and thus represent

[11] While the [Fe XIV] λ5303 line seen by Seitenzahl et al. (2019) is also within the bandpass, the lines strengths listed in Dopita et al. (2019) indicate [Fe II] dominates by at least a factor of 6.

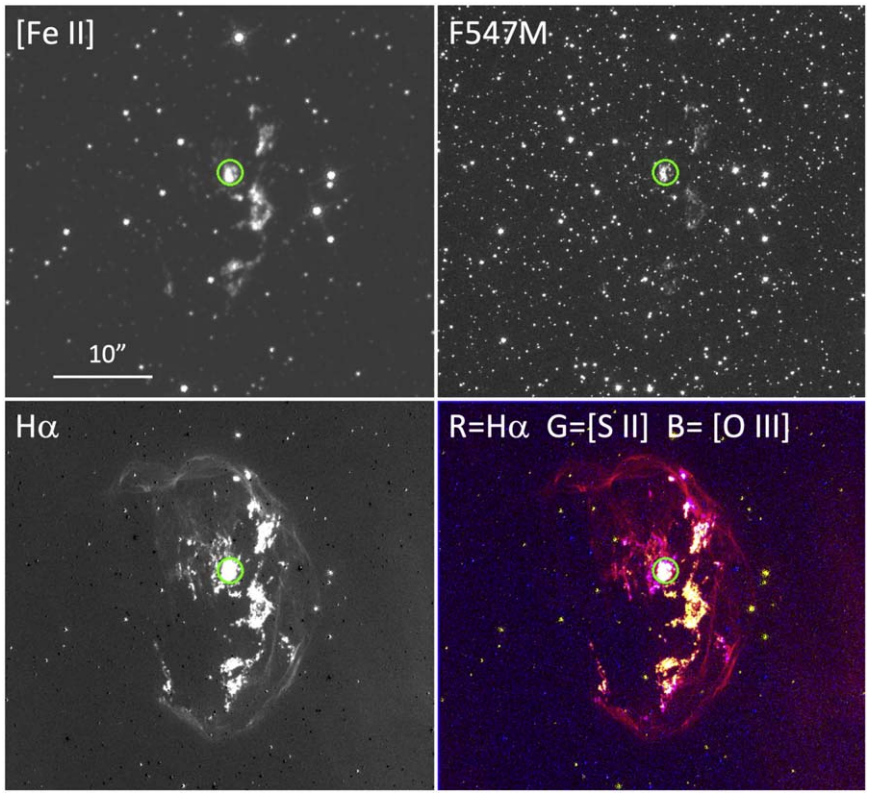

Figure 2. Four-panel figure showing aligned images of a 40″ region of HST WFC3 imagery centered on N103B. The panels show (upper left-hand panel) [Fe II] 1.644 μm, (upper right-hand panel) F547M, (lower left-hand panel) Hα, and (lower right-hand panel) a color frame with Hα in red, [S II] in green, and [O III] in blue. The emissions shown in yellow and white are radiative filaments, while the red outer shell shows the nonradiative main blast wave. The green circle shows the position and size of the COS aperture.

emission from radiative knots and filaments from slower secondary shocks being driven into density enhancements encountered by the primary shock. The larger pixel size of the IR camera (0.″13) compared to UVIS (0.″04) is obvious in the resolution of [Fe II] panel, but it is clear that we are seeing [Fe II] emission only from the radiative shock regions and not the nonradiative shocks.

The green circle in Figure 2 shows the position of the COS aperture, which was used to observe the same bright central knot of emission whose optical spectrum was observed by Dopita et al. (2019) and Li et al. (2017). Figure 3 shows a zoom into this small region, showing the same data as in Figure 2 but with the display scaled to show the detailed structure in the brightest emission. It is clear from Figure 3 that the emission sampled by the COS aperture is very complex and likely includes emission from a range of shock velocities and densities. Since the emission being passed by the F547M filter is likely dominated by several faint [Fe II] lines, this emission represents a higher spatial resolution version of what is being observed at higher signal-to-noise ratio in [Fe II] λ1.644 μm. This emission is morphologically almost identical to the Hα emission of the knot, which demonstrates how closely the [Fe II] emission is tracing the radiative shocks in this region. In Figure 4, we zoom in one more time, and simplify the display to show only the [O III] and Hα emission, highlighting the subarcsecond variations in ionization structure with the filaments observed with COS.

In general, the character and morphology of the optical filaments in N103B are very reminiscent of what is seen in Kepler's SNR (Sankrit et al. 2008), a similarity that has been noted previously (Williams et al. 2014). Figure 5 shows two additional examples of small regions of radiative filaments, which are enlarged to show their detailed structures. The top panels show Region 1, which is a small region of knotty filaments on the SW limb, seen (at least in projection) within some of the smooth, faint nonradiative filaments from the main blast wave. In the color panel, these filaments are primarily red, which means that they are strong in Hα. However, there are subtle color differences, with magenta filaments including some [O III] emission and a couple of orange knots toward the north, which means that some [S II] emission is also present. These are presumably density enhancements that have been struck by the main blast wave relatively recently and are in the early, incomplete stages of transition to becoming radiative. The northern (orange) filaments are the only ones that show significant [Fe II] emission, which is consistent with the idea that these filaments are farther along toward becoming fully radiative. Again, the presence of these transition filaments is very similar to what has been seen in Kepler's SNR (Blair et al. 1991), the only other SNR for which this morphology has been observed.

The bottom panels of Figure 5 show Region 2, which is a grouping of well-developed radiative filaments just to the SW of the COS position (i.e., seen in projection much closer to the center of the remnant). Li et al. (2017) refer to these filaments as their grouping III. The color variations seen in the right-hand panel show that the relative fluxes of the various emission lines are changing, but it is not clear how much of this may be due to

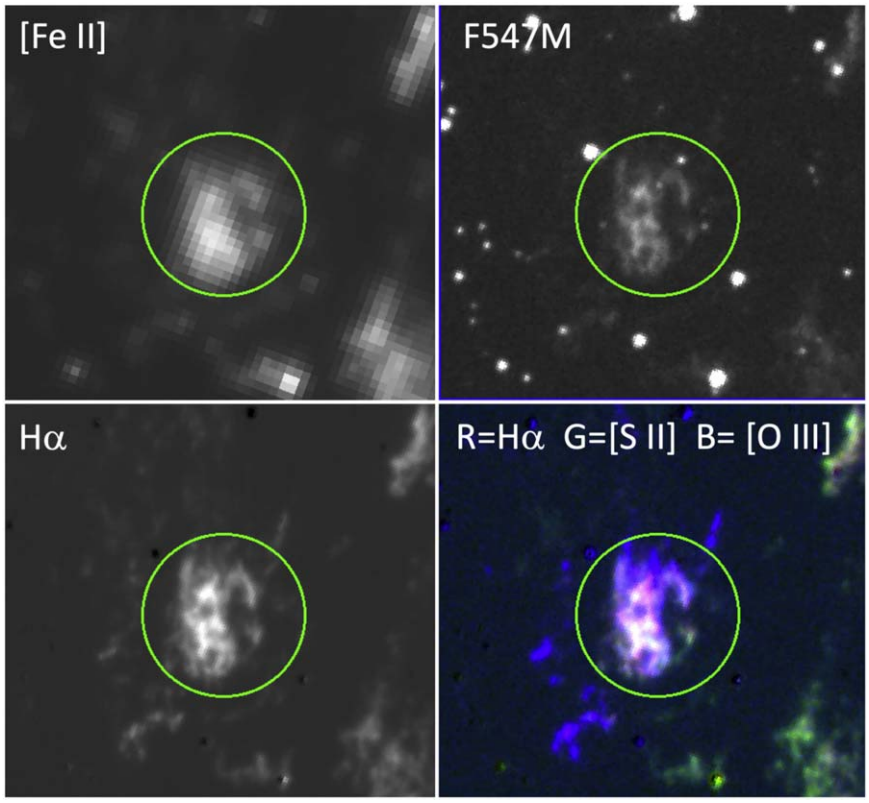

Figure 3. Four-panel figure of a 6″ region centered on the COS 2.″5 diameter aperture position. The panels are the same as in Figure 2 but the scaling has been adjusted to show the detail in the bright filaments. The faint emission filaments seen in the F547M continuum frame are likely to be due to faint [Fe II] lines that lie within the filter bandpass. They represent a higher spatial resolution version of the brighter [Fe II] 1.644 μm emission seen directly in the upper left-hand panel. Note the complexity of the emission knot sampled by the COS aperture, with different colors indicating varying ratios of the relative line intensities.

changing physical conditions (variable density and hence effective shock velocity) and how much may be due to shock incompleteness effects (variable time since a given filament encountered the primary shock). The same complexity probably occurs in the bright feature observed with COS but on a compressed spatial scale, at least as seen in projection.

2.2. COS FUV Spectroscopy

The 2.″5 point source aperture of COS was placed on the bright central knot in N103B, as shown in Figure 2. Table 1 includes the observational details. The COS G140L grating was used at all four FP-POS positions to produce a spectrum covering the range 900–2000 Å, although the data below ∼1150 Å and above 1950 Å are too noisy for use. The data were processed with the standard pipeline processing via CalCOS v2.12. These data were obtained at COS lifetime position 3, for which there are some complications for extended sources that fill the 2.″5 aperture; some flux may be lost at locations where the extended source emission overlaps a low-sensitivity portion of the detector. However, while Figure 3 shows the bright knot to be resolved, the bright emission does not fill the aperture entirely. Our assessment of relative line intensities below seems to indicate that the impact is small, but this adds some uncertainty to the interpretation of relative line intensities.

The FUV line intensities and line widths have been measured using a Python-based Gaussian fitting routine. Values and 1σ errors are provided in Table 2. We apply the Fitzpatrick (1986) average LMC extinction curve with a value of $E(B-V) = 0.33$ (determined from the optical Balmer lines—see below) to deredden the spectrum.[12] The derived intrinsic fluxes are also shown in Table 2, both in physical units and scaled relative to [O III] λ1666 = 100. These scaled intensities will be compare with the model calculations later on. In Figure 6, we show a version of the spectrum with the extinction correction applied that also shows the line identifications.

Because of the extended nature of the emission within the aperture, the spectral resolution achieved is lower than that expected for a point source. Based on measurements of the strong [O I] airglow line at 1356 Å, we find the width of an emission line filling the COS aperture to be 7.9 Å. While emission certainly fills the COS aperture, the brightest emission is more compact and hence observed SNR lines are somewhat narrower, depending on the internal kinematics of the emitting material. For example, He II λ1640 is a strong, single line and shows a FWHM of 4.4 Å, or about 800 km s^{-1}. With shock velocities near 200 km s^{-1} derived below, it is clear we are not resolving actual kinematic information from these low-resolution data.

A low-level but significant continuum is present in the COS spectrum. Some fraction of this component may be due to hydrogen two-photon continuum, as shown by the dashed line in Figure 6 (see the discussion later on), but the continuum peaks at shorter wavelengths than expected for the two-photon continuum, and it extends to the short-wavelength side of Lyα, possibly even showing a broad Lyα absorption line. It seems likely that a significant fraction of this continuum is simply

[12] Lewis et al. (2003) report an N(H) absorption column in X-ray of (3–4) × 10^{21} cm^{-2}, consistent with a moderately high extinction on this line of sight.

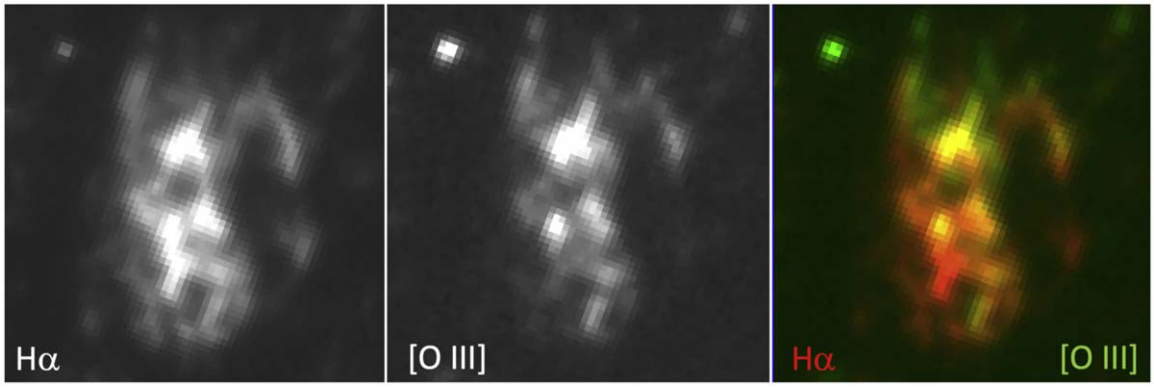

Figure 4. Comparison of the subarcsecond structure of the bright filament observed with COS, as viewed in Hα + [N II] (marked "Hα") (left-hand panel), [O III] λ5007 (center panel), and colorized (right-hand panel). The region shown is 2.″5 square. Using the average line intensities from the optical spectrum, we can convert the ratios observed in these filters to the equivalent [O III] λ5007 to Hβ ratio, which is less reddening dependent. Regions appearing green (top of Figure) have λ5007:H$\beta \sim 2.2$ while the bright red region below center has ratio 0.33. The bright yellow knot above center has λ5007:H$\beta \simeq 1.4$.

scattered starlight from the general region of the LMC bar, as noted in the far-UV spectrum of N103B from FUSE (see Blair et al. 2006, Appendix A6 and Figure 7), although the aperture in that case was significantly larger. A close inspection of the F547M panel in Figure 3 shows a few faint spoiler stars within the aperture that could also be responsible for this faint continuum.

3. Analysis

3.1. Additional Information on the Bright Knot's Emission

Dopita et al. (2019) provided a full set of optical extinction-corrected line intensities for the central knot in N103B (see their Table 8). However, not knowing exactly what region was extracted for their spectrum, we have instead re-extracted some of the key observed optical line intensities from the WiFeS data (Proposal ID: 4140118, PI Seitenzahl) for use here. Using QFitsView (Ott 2012), we inspected the WiFeS data cube and selected a 3 × 3 spaxel region that not only approximated the COS aperture size but also encapsulated the emission of the bright knot with a minimum of contamination from nearby emission. WiFeS spaxels are essentially 1″ square. Therefore, the listed optical fluxes are effectively surface brightnesses per square arcsec averaged over the nine spaxels that were extracted. We use the observed ratio of the Balmer lines with the Cardelli et al. (1989) extinction curve to determine $E(B-V) = 0.33$ (assuming $R = 3.1$), and then apply this correction to the observed optical line intensities to obtain intrinsic relative intensities, as shown in Table 2.[13] The relative scaling between the optical and COS FUV lines is complicated by a number of factors, such as the very different spatial resolution and somewhat different aperture sizes, as well as the large separation in wavelength. Therefore, we decided instead to work with relative line intensities within each wavelength range as much as possible. In the bottom section of Table 2, we show the optical lines for the COS knot scaled relative to I (Hβ) = 100 for comparison to the models.

We also extracted the fluxes within the projected COS aperture from each of the WFC3 images. Besides providing a simple sanity check on fluxes, this allows us to scale the [Fe II] λ1.644 μm line intensity into the comparison in a reasonable way. The IRAF[14] task "imexamine" was used to derive total counts in the projected COS aperture from each WFC3 filter image. These counts were then converted to fluxes using conversion factors derived from the file headers. We find F([Fe II]) = 9.22 × 10^{-14} erg cm^{-2} s^{-1}; F([O III]) = 9.85 × 10^{-14} erg cm^{-2} s^{-1}; F([S II]) = 9.58 × 10^{-14} erg cm^{-2} s^{-1}; and F(Hα) = 5.68 × 10^{-13} erg cm^{-2} s^{-1}. The [Fe II] image flux was scaled to the [O III] image flux (since it is a single line), and then scaled to the optical relative line intensities to obtain the relative scaling shown in Table 2.

According to Li et al. (2017) the emission from the COS position is redshifted by nearly 400 km s^{-1} (which is ∼150 km s^{-1} with respect to the LMC local ISM). This means that the resonance lines C IV, Si IV, N V, and C II are nearly unaffected by resonance scattering in the ISM of either the Milky Way or the LMC, which would otherwise cut into the short-wavelength sides of their profiles. This is consistent with the results of the Gaussian fits to the line profiles, which imply little asymmetry in the lines. From Figure 8 of Li et al. (2017), we estimate that no more than 10%–15% of the resonance-line flux can be missing. Hence, given other uncertainties, it is reasonable to use the extinction-corrected FUV line intensities with the WiFeS optical observations of the filament to compare to shock-model calculations.

Sano et al. (2018) detect two small clumps of CO emission (see their Figure 7) in addition to the larger molecular cloud emission to the south and east of N103B. Their "clump A" is centered ∼3″ northeast of the COS aperture and the contours partially overlap the bright knot observed with COS. They measure a physical size of this clump as ∼1.2 pc and estimate a mass of over 100 $M_{\odot}$. However, the velocity of this emission is consistent with the LMC rest frame (∼246 km s^{-1}) and not with the velocity of the bright knot (centered at 385 km s^{-1}). We do not consider this to be a physical association but rather a projection effect. Likewise, while their "clump B" overlaps the southwest limb of the SNR, we see no evidence of deformation of the shock front at that location that would indicate a physical interaction with the CO-emitting clump.

[13] The LMC and galactic extinction curves are very similar over the optical wavelength range, but different in the UV due to a larger number of small grains in the LMC; hence, the use of the Fitzpatrick (1986) curve for the COS spectrum.

[14] IRAF is distributed by the National Optical Astronomy Observatory, which is operated by the Association of Universities for Research in Astronomy, Inc., under cooperative agreement with the National Science Foundation.

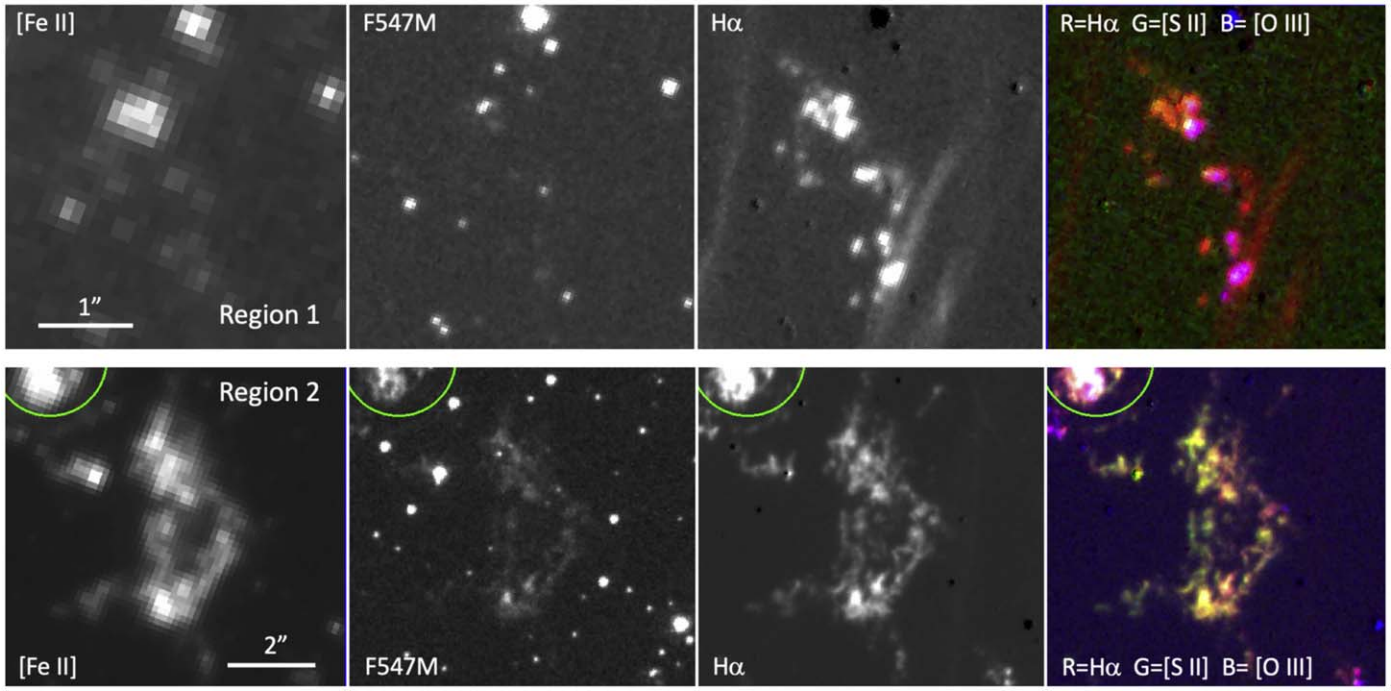

Figure 5. This figure shows two regions of clumpy, radiative filaments in N103B that have very different emission properties. The top four panels show Region 1, a 4″ region centered ∼9″ SW of the bright central knot, near the SW limb of the SNR. It shows knotty filaments primarily seen in Hα; minor admixtures of [O III] (magenta) and/or [S II] (orange) indicate these are knotty nonradiative filaments in the early stages of transition to becoming radiative. The bottom four panels show Region 2, a 7″ region of brighter radiative filaments just a few arcsec to the SW of the COS aperture position. These filaments are well on their way to establishing full cooling and recombination zones but the relative line strengths vary, which causes the color variations. Note how the [Fe II] emission has "turned on" for these filaments. This same complexity is happening within the region observed with COS but on a more compressed spatial scale.

3.2. Comparison to Model Calculations

To interpret the combined COS and optical/IR data, we have calculated shock models using the code that was first described by Raymond (1979), which has been continually updated with improved atomic physics and functionality over the years (see Cox & Raymond 1985; Hartigan et al. 2004; Koo et al. 2016, and references therein). The line width observed by Li et al. (2017) in the broad Hα component of the brightest nebular knots is 190 km s^{-1}, which is consistent with shock speeds of 200 km s^{-1} or more. A number of preliminary models were calculated to constrain the relevant range of preshock density and magnetic field parameters that reproduced the approximate observed postshock density-sensitive line ratios, which all indicate very high densities. The optical [S II] $\lambda\lambda$6717, 6731 ratio is in the high-density limit, and the [S II]:Hα ratio is 0.22, which is low for typical radiative SNR shocks. This indicates that significant collisional de-excitation of the [S II] lines is responsible for the low observed ratio. However, other diagnostics are available (Dere et al. 1997), such as the Si III ratio $I(\lambda1885)/I(\lambda1894)$ and C III ratio $I(\lambda1176)/I(\lambda1909)$, which indicate densities of $3 - 10 \times 10^4$ cm^{-3}.[15] The optical [S II] $\lambda4075/\lambda6725$ ratio also indicates that a high density is needed to match the observations. Postshock densities can be varied in the models by either increasing the assumed preshock density or by adjusting the assumed magnetic field, which adjusts the compression in the postshock flow. (Lower magnetic fields allow more compression and thus higher densities at a given location in the postshock flow.)

The results of three models are shown in Table 2, where the FUV lines are scaled (as with the observations) to O III] $\lambda1666 = 100$ and the optical lines are scaled to H$\beta = 100$. Models A, B, and C were calculated assuming shock velocities of 200, 220, and 250 km s^{-1}, preshock densities 3100, 1370, and 1000 cm^{-3}, magnetic field strengths 180, 300, and 180 μG, respectively, and fully preionized preshock gas. We used the abundances that Dopita et al. (2019) derived for N103B as a starting point for these models, viz. He, C, N, O, Ne, Mg, Si, S, Ar, Ca, Fe, Ni = 10.92, 8.09, 7.17, 8.37, 7.57, 7.19, 7.11, 6.88, 5.79, 6.02, 7.33, and 5.91, respectively. A photoionization precursor may contribute to some of the lines, but the contribution is modest (Vancura et al. 1992), and following Dopita et al. (2019) we do not include it.

Model B is intended to be similar to the model calculated with the MAPPINGS code by Dopita et al. (2019) for N103B, with a shock speed of 220 km s^{-1} and a ram pressure of 1.33×10^{-6} dyne cm^{-2}; they assumed equipartition of thermal and magnetic pressure ahead of shock. The abundances seem to work well overall and their derived parameters produce a reasonable fit to the data, especially given that it is for a single shock velocity. Most lines are within 20% of the observed relative fluxes. The exceptions are none other than the two density-sensitive ratios mentioned earlier, both of which indicate higher densities than given in Model B by at least a factor of 2. Our models A and C use a lower magnetic field strength in part to address this discrepancy. At T $\simeq$ 30,000 K in the cooling zone of the models, Model A has $n_e = 1.2 \times 10^5$ cm^{-3}, Model B has $n_e = 2.5 \times 10^4$ cm^{-3}, and Model C

[15] Interestingly, the Si III lines are adjacent in wavelength while the C III lines are widely separated. Hence, another way to look at this is that the consistency for the density estimates from these two line ratios argues that the extinction correction is approximately correct.

Table 2
HST/COS and Key Optical[a] Emission-line Fluxes for N103B Compared to Models

Ion	λ[b] (Å)	Flux (erg cm^{-2} s^{-1})	Width[c] (Å)	Intensity[d] (ergs cm^{-2} s^{-1})	Scaled Int.[e]	Model A[f] $V = 200$	Model B[f] $V = 220$	Model C[f] $V = 250$
[Ne V]	1147.25	3.3 ± 0.6E-16	2.2 ± 0.2	4.0E-14	14	67	71	74
C III	1175.94	7.1 ± 0.7E-16	5.1 ± 0.3	6.8E-14	25	36	17	19
Si III?	1201.18	2.5 ± 0.5E-15	8.7 ± 1.0	2.0E-13	77	88	84	87
N V	1241.82	2.3 ± 0.3E-15	5.1 ± 0.1	1.4E-13	57	69	76	75
C II	1336.69	2.5 ± 0.7E-15	4.1 ± 0.1	9.8E-14	43	94	102	110
O V	1373.20	1.6 ± 0.2E-15	4.6 ± 0.1	5.5E-14	25	35	33	35
Si IV	1395.29	3.0 ± 0.5E-15	3.9 ± 0.1	9.6E-14	44	23	17	22
O IV]	1404.40	9.6 ± 1.3E-15	6.7 ± 0.3[g]	3.0E-13	137	225	206	221
[Si VIII]	1441.95	6.0 ± 0.8E-16	3.4 ± 0.3	1.7E-14	8	0.4	1	25
N IV]	1484.75	1.5 ± 0.3E-15	8.2 ± 0.5	3.8E-14	18	18	17	17
C IV	1550.59	2.7 ± 0.3E-14	5.3 ± 0.05	6.1E-13	294	402	376	394
Fe II	1603.17	1.0 ± 0.1E-15	2.6 ± 0.1	2.1E-14	10	…	…	…
He II	1642.03	1.9 ± 0.3E-14	4.4 ± 0.05	3.9E-13	189	175	232	342
O III]	1666.00	1.0 ± 0.1E-14	6.5 ± 0.2[g]	2.0E-13	100	100	100	100
Si II	1817.39	2.6 ± 0.4E-15	4.9 ± 0.2	5.0E-14	26	3	4	6
[Si III	1885.23	3.2 ± 0.7E-15	4.1 ± 0.2	6.3E-14	31	17	43	39
Si III]	1894.41	4.6 ± 0.6E-15	5.1 ± 0.2	9.1E-14	44	35	39	39
C III]	1909.74	1.9 ± 0.3E-14	5.1 ± 0.1	3.8E-13	188	188	241	268
Cont.[h]	(1450)	3.84E-13	…	1.01E-11	4960	920	1050	1730
[O II]	3727	8.72 ± 0.14E-15	4.54 ± 0.05	3.71E-14	206	55	189	180
[Ne III]	3869	1.53 ± 0.03E-15	3.19 ± 0.04	6.30E-15	35	70	44	49
[S II]	4075	2.79 ± 0.03E-15	3.20 ± 0.05	1.09E-14	61	58	33	38
He II	4686	2.83 ± 0.08E-16	3.74 ± 0.04	9.06E-16	5	8	12	12
Hβ	4861	6.01 ± 0.03E-15	3.86 ± 0.03	1.80E-14	100	100	100	100
[O III]	5007	5.13 ± 0.04E-15	4.11 ± 0.04	1.47E-14	82	150	245	222
[O I]	6300	6.79 ± 0.08E-15	4.12 ± 0.03	1.55E-14	86	65	50	75
Hα	6563	2.45 ± 0.02E-14	4.83 ± 0.06	5.31E-14	295	295	295	295
[N II]	6584	4.33 ± 0.06E-15	4.49 ± 0.20	9.31E-15	52	40	65	70
[S II][i]	6725	5.45 ± 0.08E-15	4.40 ± 0.04	1.15E-14	64	54	86	83
[Fe II][j]	16440	4.80E-15	…	5.76E-15	32	277	279	346

Notes.
[a] Optical line intensities scaled per square arcsec from Dopita et al. (2019) WiFeS spectrum with our adopted extinction correction applied; see text.
[b] Measured central wavelength.
[c] FWHM from Gaussian fit to each line.
[d] Intrinsic flux after correction for extinction; see text.
[e] Relative intensity scaled to I(O III] 1666) = 100 (UV) and I(Hβ) = 100 (optical).
[f] For full description of model assumptions, see text.
[g] Blend of multiple components; Gaussian width not representative.
[h] Intensity columns give integrated continuum flux; models give expected hydrogen two-photon continuum flux.
[i] The [S II] doublet ratio λ6717/λ6731 is 0.46, in the high-density limit.
[j] [Fe II] flux from F164N image appropriately scaled to optical spectrum; see text.

has $n_e = 2.9 \times 10^4$ cm^{-3}, giving Si III ratios of 0.49, 1.48, and 1.0, respectively, bracketing the observed ratio of 0.70.

Also recall that the observed complexity of the bright knot (see Figure 3) makes it likely that a range of shock conditions is actually present within the aperture. However, the brightest radiative shocks near 220 km s^{-1} apparently dominate the observed emission, making even single-velocity models in this range acceptable to constrain abundances, as was recently found for the Cygnus Loop (Raymond et al. 2020). Some of the weaker lines from the highest ionization states hint at more complexity, but of course their observed strengths are also more uncertain. The weak [Si VIII] λ1442 line nominally requires a faster shock, but that would produce too much flux in the He II λ1640 and λ4686 lines. Given the weakness of the [Fe VII] optical line, it is likely that grain destruction is incomplete at the temperatures where Si VIII and Fe VII are formed, so the range of shock speeds must include speeds above 250 km s^{-1}.

Dopita et al. (2019) had no solid diagnostics for the C and Si abundances, but adopted reasonable values from other published work. The observed Si IV λ1394 line is stronger than the models, while the Si III $\lambda\lambda$ 1885,1892 lines agree reasonably well. (The identification of Si III λ1206 is considered uncertain due to the strong Lyα airglow feature.) C IV λ1550 is overpredicted by the models, while C III λ1909 line is approximately correct in the models that reproduce the λ1176/λ1909 ratio.[16] C II λ1335 is predicted to be too strong, but it is such a strong resonance line that, of all the permitted transitions, it might be somewhat attenuated by ISM scattering. Overall, this suggests that the assumed abundances for those elements are approximately correct if grains are completely destroyed by the time the gas cools to 10^5 K. We note that the [Fe II] 1.644 μm line is substantially overpredicted, which

[16] Recall, however, that the uncertainty in the weak λ1176 line and the reddening correction both impact this comparison.

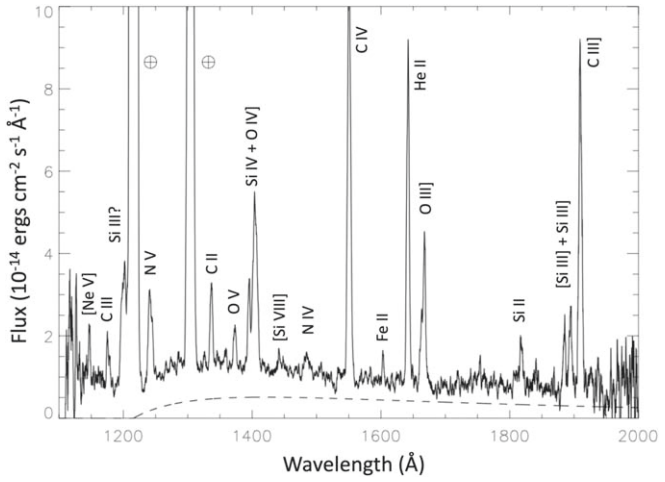

Figure 6. The COS spectrum is shown after correction for reddening, as described in the text. The line identifications are shown. The dashed line indicates the shape of the 2-photon continuum spectrum for reference, which was calculated for a 250 km s^{-1} shock. However, neither the shape nor the strength of the continuum is well-matched by two-photon alone, implying that blue starlight is present at a low level. See text for details.

suggests the possibility of a lower Fe abundance or incomplete Fe grain destruction relative to C and Si, though the collisional excitation rates for [Fe II] lines are somewhat uncertain. Shocks at these speeds are expected to return about half of the iron to the gas phase (Dopita et al. 2016). In addition, the models are allowed to cool to 1000 K, and [Fe II] forms in the final stages of that cooling. Since it takes almost 700 yr for the gas to reach 1000 K, and since the bright radiative shocks have effective ages much less than the age of the SNR, incomplete cooling is very likely to be the cause of this discrepancy.

The assumed N:O abundance ratio gives an excellent match to the N V and N IV] lines relative to the O lines, which confirms the finding of Dopita et al. (2019) of an ordinary ISM abundance of N. We have only an upper limit on H from the 2-photon continuum but if H had been burned to He, then the λ1640 line would be much stronger than observed. Therefore, it seems that there is no evidence for nuclear burning of the material being encountered by the shock. The abundances in the bright knot thus look to be entirely consistent with expectations from the interstellar gas in the LMC.

Finally, although we concentrate here on the FUV spectrum, we note one glaring discrepancy with the predicted optical lines: the [O III] $\lambda\lambda$4959, 5007 lines are predicted to be too bright by a factor of 2. This appears to be a generic problem in modeling. Dopita et al. (2016) modeled the spectrum of the LMC remnant N49 with a single shock of 250 km s^{-1} and found that the same factor-of-2 discrepancy in [O III] appeared in an otherwise reasonable model match. This discrepancy may be an indication of thermally unstable cooling (e.g., Innes 1992; Sutherland & Dopita 1993) because unstable cooling tends to shift energy from higher to lower temperature regions. It might also indicate that slower shocks, as seen in the regions of high Hα to [O III] ratios in Figure 3, make a substantial contribution.

Given the complexity of the filament being observed with COS, it is quite surprising how well a single-velocity model (or at least a modest range of shock velocity models) can reproduce the observed spectrum. Referring to Figure 4, it is possible that the brightest optical filaments dominate the lower ionization lines, while the fainter (but higher ionization) filaments seen primarily in [O III] actually dominate the FUV emission. When viewed without the benefit of the full spatial resolution of HST, the combined spectrum approximates a fairly fast and complete shock reasonably well. But clearly this is an oversimplification of a more complex interaction between the shock and the bright knot at the COS position.

Overall, we find that the abundances used by Dopita et al. (2019) work well within the combined uncertainties of the observations and the models. However, Dopita et al. (2019) do not consider how much variation in abundances could be present while still providing a reasonable match to their model. Abundance uncertainties are difficult to assess quantitatively, due to the way various parameters besides abundances can interact in the models that predict the line ratios, but the presence of multiple ionization stages of various ions can at least bound the problem to some degree. In Appendix, we provide a more detailed discussion of this process and we derive the following constraints. If we adopt measurement uncertainties of 25% in the UV line ratios and add these in quadrature with the uncertainties discussed in Appendix, then we arrive at the following abundance estimates and ranges relative to Dopita et al. (2019) (represented by D19): N:O = D19 $\times$ 1.1 $\pm$ 0.35; C:O = D19 $\times$ 0.8 $\pm$ 0.47; Si:O = D19 $\times$ 0.5 $\pm$ 0.40; and from the optical, N:H = D19 $\times$ 1.0 $\pm$ 0.5. Note that this estimate would allow some modest amount of enhancement in N:H over ISM abundances, although this is not required by the observations.

3.3. Geometry of the Observed Filament

The observed redshift of the filament relative to the LMC velocity, as observed by Li et al. (2017), must result from some combination of Doppler velocity and line-of-sight projection angle, θ. The range of velocities that they see could then result from a range of these parameters within the sampled material, which seems likely given the complex morphology of the filament. Two possibilities occur to explain the overall redshift. Either the cloud was moving at fairly high velocity before the shock arrived, or the cloud is seen fairly face-on (but moving away from us) rather than edge-on and has been accelerated by the shock. The former case would suggest ejection from the progenitor system, while the latter would require a range of shock speeds.

We can eliminate the possibility that the cloud itself was moving at $\sim$200 km s^{-1} before the blast wave hit it in the following manner. As seen in N49 by Vancura et al. (1992), there should be a photoionization precursor visible as a narrow component of Hα. From Li et al. (2017), it appears that there is a narrow component at the LMC rest velocity, but there is no narrow component emission offset 200 km s^{-1} (their Figure 8) corresponding to the bright knot. Adopting the latter approach, the peak is about 150 km s^{-1} redward of the narrow LMC component. Taken at face value, this means that we are looking at the cloud a little ways from face-on (albeit from the rear since it is moving away from us), with cos(θ) $\sim$0.6. As the gas cools, it is moving at the shock speed, so a 300 km s^{-1} shock is enough to account for this velocity. This geometry is consistent with the lack of apparent resonance-line scattering, which might have been expected from shocks being viewed closer to edge-on. From the velocity perspective, this geometry means that the highest velocity emission in the profile, which is seen at $\sim$540 km s^{-1}, or 300 km s^{-1} redward of the LMC rest velocity, requires some shocks up to $\sim$500 km s^{-1} to be present.

4. Discussion and Comparison with Kepler's SNR

Despite the larger age and diameter of N103B, the similarities between it and Kepler's SNR in our Galaxy are truly remarkable, as discussed by Williams et al. (2014). Both show a primary shock front demarcated by Balmer filaments and clumpy radiative shock emission from secondary shocks driven into density enhancements. Both are expanding into surrounding material characterized by high densities and a density gradient; while most other remnants of SN Ia's are expanding into very low density regions (see Williams et al. 2014, Table 3). The Spitzer IRS spectra of the two objects are nearly identical, showing warm dust heated by the primary shock and an anomalous broad silicate feature centered near 17.2 μm, the latter is taken as evidence of circumstellar dust in the outflow from the pre-supernova system (Henning 2010). This conclusion seems particularly strong for Kepler, whose position hundreds of parsecs off the galactic plane makes a circumstellar origin of the material highly favored. It is difficult not to conclude the same thing for N103B. This is our favored explanation.

Our findings in this paper from analysis of both optical and FUV spectral data of N103B have only solidified the view that the material being encountered by the shock has chemical abundances that are consistent with those expected for the local ISM. Interestingly, this confirms yet another similarity with Kepler. Dopita et al. (2019) have now shown quite conclusively that the abundances in the radiative knots of Kepler's SNR are also consistent with those expected for the local ISM abundances at its location only $\sim$3 kpc from the galactic center, this point was first noted in Blair et al. (2007). We mention this because there continues to be confusion on this point, even in recent literature for Kepler (see Li et al. 2017; Sano et al. 2018; Millard et al. 2020). The confusion is caused by the high observed N abundance in the shocked material in Kepler (Blair et al. 1991), which over the years has been attributed incorrectly to an enhancement in the circumstellar medium (CSM) from the progenitor system instead of it being a reflection of the abundance gradient in our Galaxy (Rolleston et al. 2000; Rudolph et al. 2006).

So what are the implications of the normal ISM abundances in the dense, knotty material around both N103B and Kepler? Either (a) the material is truly ISM material, or (b) it is circumstellar (i.e., from the progenitor system) but with abundances consistent with normal ISM. Dopita et al. (2019) adopt the former conclusion, which ignores the significant evidence pointing to a circumstellar origin of the material being encountered by the shock, especially for Kepler. We note that N103B is located in the outskirts of a large shell of emission that surrounds the nearby cluster NGC 1850. As Sano et al. (2018) point out, there are molecular clouds in the vicinity, and their Figure 1 shows the presence of very faint, diffuse Hα emission in the wider field surrounding N103B (see also Figure 1 in Li et al. 2017, for an even wider view). Hence, it is perhaps less compelling that the material surrounding N103B must have originated from the progenitor system. Were it not for the many similarities to Kepler's SNR and its probable CSM interaction, this might be the preferred conclusion.

Adopting conclusion (b) above implies that the material lost in the pre-SN wind phase for both Kepler and N103B was not heavily enriched or processed by the precursor system. This conclusion has obvious implications for the precursor system. For example, single-degenerate models where the companion was a red giant (RG) or asymptotic giant branch (AGB) star would not be favored because the CSM produced from those systems would be expected to have enhanced N over the ISM abundances (Chiotellis et al. 2012). Searches for the surviving companion in Kepler have largely ruled out brighter possibilities such as RG and AGB companions (Kerzendorf et al. 2014; Ruiz-Lapuente et al. 2018), but possible surviving companions from fainter main sequence or even sub-dwarf or white dwarf companions have been proposed but not yet ruled out (Marietta et al. 2000; Shen & Schwab 2017; Meng & Li 2019). A number of models for single-degenerate SNIa exist that involve main sequence companions (Han & Podsiadlowski 2006; Meng & Yang 2010) or common envelope phases (Kashi & Soker 2011; Meng & Podsiadlowski 2017) that can lead to a significant mass loss but avoid the need for enhanced abundances in the resulting CSM, but these scenarios have not been explored in detail. It is also likely even in the CSM scenario that some significant amount of ISM will have been swept up and mixed in with the CSM by the time that these remnants have grown to several parsecs in radius, thus diluting any abundance anomalies.

One other significant clue might lie in the mass of the material in the purported CSM component. In their analysis for Kepler, Dopita et al. (2019) use the observed densities and physical size of the bright western radiative filament grouping in Kepler to estimate that it likely contains several $M_\odot$ of material. Blair et al. (2007) estimated nearly a solar mass of material was involved in the currently heated material in the shell of Kepler. For N103B, Williams et al. (2014) use X-ray and IR data to estimate $\sim$3 $M_\odot$ of material currently emitting. For the bright COS filament, the models we have presented show that the assumed preshock density and magnetic field strength play off against each other, but reasonable assumptions about the size, depth, and density can be used to arrive at an estimate of order 0.1 $M_\odot$. Li et al. (2017) performed a similar experiment using most of the bright filaments and concluded that at least 1 $M_\odot$ of material is present (with even more if previously shocked material has already cooled). Overall, this seems comparable to the situation in Kepler. These estimates thus require a significant amount of mass loss from the progenitor system if the CSM option is to be believed. Some of the models investigated by Meng & Yang (2010) have appropriately massive companions that could provide this material if sufficient mass can indeed be lost in the pre-SN phase. Alternatively, if this is really ISM, then one needs to account for why such a dense, structured ISM exists around these SNRs.

While we favor the CSM interpretation, we are unfortunately left with a conundrum as to the true origin of the material being encountered by the expanding blast wave in N103B. The best way to potentially resolve this issue is to determine whether a fainter surviving companion can be identified. This would then inform the discussion of what the progenitor system might have been and thus what any material lost from that system might have been like. The star indicated by Li et al. (2017) is certainly not an ironclad identification of a companion, but follow-up work is needed. Also, assuming that fainter companions are in play, there are numerous other stars near the center of N103B that were not considered by Li et al. (2017). Any search for a surviving companion should reconsider the assumed position of the explosion in determining the region to be searched. Li et al. (2017) selected the center of an ellipse fit to the partial Hα shell as

their center position. From consideration of hydrodynamic models of expanding winds into a surrounding medium with a density gradient, such as those of Wareing et al. (2007), it seems likely that the explosion site could be significantly closer to the apex of the bow shock represented by the partial shell (e.g., west of the currently assumed center; see Figure 3 of Wareing et al. 2007).

5. Summary

We report new, high spatial resolution HST/WFC3 imagery of N103B in the LMC, and HST/COS FUV spectroscopy of the brightest radiative emission knot near the projected center of the SNR. The images show the extent and structure of the faint Balmer-dominated filaments from the primary blast wave that form a partial shell, as well as bright clumpy radiative shock filaments projected within this shell that represent secondary shocks being driven into density enhancements. These radiative filaments show a range of relative line intensities that likely arise both from a range of physical conditions (e.g., densities and shock velocities) and effective ages (i.e., times since encountering the primary blast wave). Some of these filaments represent material in transition to becoming fully radiative, while others appear to have established more complete cooling and recombination zones.

Our COS data for the brightest radiatively emitting knot, which itself shows complex structure at HST resolution, presents a rich FUV spectrum and faint underlying continuum. Modeling the emission-line strengths, along with existing optical data for this filament shows the emission to be dominated by fast radiative shocks into material with abundances consistent with local LMC ISM. We point out the similarity between N103B and Kepler's SNR, where the conclusion that the material being encountered by the shock is circumstellar material shed by the precursor system seems secure, and we consider that this is also likely for N103B. Under this assumption, the normal abundances seen to imply a precursor system that did not produce an enhancement in abundances at a level detectable in our measurements. We encourage additional effort to search for and/or confirm a possible surviving companion star as a way to better understand the progenitor to this SNe Ia.

Partial support for the analysis of the data was provided by NASA through grant No. HST-GO-14359 from the Space Telescope Science Institute, which is operated by AURA, Inc., under NASA contract NAS 5-26555. CHIANTI is a collaborative project involving George Mason University, the University of Michigan (USA), University of Cambridge (UK) and NASA Goddard Space Flight Center (USA). P.F.W. acknowledges additional support from the NSF through grant AST-1714281. W.P.B. acknowledges partial support from the JHU Center for Astrophysical Sciences. I.R.S. acknowledges funding from the Australian Research Council under grant FT160100028.

Facilities: HST(WFC3), HST(COS), ANU 2.3m(WiFeS).

Software: DS9 (Joye & Mandel 2003), IRAF, QFitsView (Ott 2012).

Appendix
Chemical Abundance Considerations

In this Appendix, we provide a more detailed discussion of the chemical abundances and their uncertainties. The models shown in Table 2 assumed the abundance set derived by Dopita et al. (2019) for the LMC ISM. Here, we use the results of the models compared with the extinction-corrected line strengths to assess how well these assumed abundances have worked for N103B.

N to O ratio from UV lines: The UV lines of N IV] and N V and of O III] and O IV] give the N:O ratio. The gas must cool through the temperature range where these lines are formed, and for shocks above 200 km s^{-1} the line ratios depend primarily on the relative abundances and the atomic rates. The excitation rates for these particular lines should be good to 20%. There is also an O V line in the COS spectral range, but it has a very high excitation potential, equivalent to $T = 3.3 \times 10^5$ K, so the uncertainty is higher for that line. With the Dopita et al. (2019) abundances, the N line ratios to O III] agree with the models, while the ratios to O IV] are about 20% too low. We estimate that the N:O ratio is 1.1 ± 0.2 times the Dopita et al. (2019) value.

N to H ratio from optical lines: The [N II] to Hα ratio depends not only on atomic rates but also on the spectrum of ionizing radiation, on radiative transfer, and on the abundances of the elements that provide competing radiative cooling. There is also a contribution from the photoionization precursor that was not included in Dopita et al. (2019) or our analysis. The magnetic field strength determines the compression ratio, and therefore the ionization parameter in the photoionized region where [N II] is formed, and this parameter is not independently known. The predicted ratios of the three models in Table 2 vary from 0.40 to 0.70, compared with an observed value of 0.55. Considering that the three models do not cover a full range of parameter space, along with reasonable guesses at the uncertainties in photoionization cross sections and radiative transfer, we conclude that the N:H ratio from the optical spectrum is consistent with Dopita et al.'s (2019) value, but it could be as much as 50% higher.

C to O ratio from UV lines: The C II line is likely to be affected by the LMC ISM absorption line, but the C III] and C IV lines are not. The ratios are again determined by the relative abundances and the atomic rates, though the C III] line can be somewhat dependent on the photoionization. The ratio of C IV to O III] suggests a depletion of 20%–30% compared to the D19 abundance ratio, while the ratio to O IV] suggests very little depletion. We conclude that the C:O ratio is lower than the Dopita et al. (2019) value by a factor of 0.8 ± 0.4.

Si to O ratio from UV lines: The Si III] to O III] ratio is consistent with Dopita et al. (2019), but the Si III] to O IV] ratio suggests a 30% depletion. The Si IV to O IV] ratio suggests a stronger depletion, closer to a factor of 10. The Si IV line is blended with the O IV] multiplet, and it may be subject to a larger uncertainty. We estimate the Si:O ratio to be 0.5 ± 0.3 times the Dopita et al. (2019) value.

All of the UV lines used above are moderately strong, but even modest errors are magnified somewhat when looking at ratios. If we adopt measurement uncertainties of 25% in the UV line ratios and add in quadrature, then we arrive at the following abundance estimates relative to Dopita et al. (2019) (represented by D19). N:O = D19 × 1.1 ± 0.35; C:O = D19 × 0.8 ± 0.47; Si:O = D19 × 0.5 ± 0.40; and from the optical, N:H = D19 × 1.0 ± 0.5.

ORCID iDs

William P. Blair https://orcid.org/0000-0003-2379-6518
Parviz Ghavamian https://orcid.org/0000-0002-9886-0839
John C. Raymond https://orcid.org/0000-0002-7868-1622

Brian J. Williams https://orcid.org/0000-0003-2063-381X
Ravi Sankrit https://orcid.org/0000-0001-8858-1943
Knox S. Long https://orcid.org/0000-0002-4134-864X
P. Frank Winkler https://orcid.org/0000-0001-6311-277X
Norbert Pirzkal https://orcid.org/0000-0003-5044-5941
Ivo R. Seitenzahl https://orcid.org/0000-0002-5044-2988

References

Badenes, C., Hughes, J. P., Bravo, E., & Langer, N. 2007, ApJ, 662, 472
Blair, W. P., Ghavamian, P., Long, K. S., et al. 2007, ApJ, 662, 998
Blair, W. P., Ghavamian, P., Sankrit, R., & Danforth, C. W. 2006, ApJS, 165, 480
Blair, W. P., Long, K. S., & Vancura, O. 1991, ApJ, 366, 484
Cardelli, J. A., Clayton, G. C., & Mathis, J. S. 1989, ApJ, 345, 245
Chiotellis, A., Schure, K. M., & Vink, J. 2012, A&A, 537, A139
Cox, D. P., & Raymond, J. C. 1985, ApJ, 298, 651
Dere, K. P., Landi, E., Mason, H. E., Monsignori Fossi, B. C., & Young, P. R. 1997, A&AS, 125, 149
Dopita, M., Hart, J., McGregor, P., et al. 2007, Ap&SS, 310, 255
Dopita, M., Rhee, J., Farage, C., et al. 2010, Ap&SS, 327, 245
Dopita, M. A., Seitenzahl, I. R., Sutherland, R. S., et al. 2016, ApJ, 826 150
Dopita, M. A., Seitenzahl, I. R., Sutherland, R. S., et al. 2019, AJ, 157, 50
Fitzpatrick, E. L. 1986, AJ, 92, 1068
Ghavamian, P., Seitenzahl, I. R., Vogt, F. P. A., et al. 2017, ApJ, 847, 122
Hachisu, I., Kato, M., & Nomoto, K. 1996, ApJL, 470, L97
Han, Z., & Podsiadlowski, P. 2006, MNRAS, 368, 1095
Hartigan, P., Raymond, J., & Pierson, R. 2004, ApJL, 614, L69
Henning, T. 2010, ARA&A, 48, 21
Heringer, E., Pritchet, C., Kezwer, J., et al. 2017, ApJ, 834, 15
Hughes, J. P., Hayashi, I., Helfand, D., et al. 1995, ApJL, 444, L81
Iben, I., Jr., & Tutukov, A. V. 1984, ApJS, 54, 335
Ilkov, M., & Soker, N. 2012, MNRAS, 419, 1695
Innes, D. E. 1992, A&A, 256, 660
Joye, W. A., & Mandel, E. 2003, in ASP Conf. Ser. 295, Astronomical Data Analysis Software and Systems XII, ed. H. E. Payne, R. I. Jedrzejewski, & R. N. Hook (San Francisco, CA: ASP), 489
Kashi, A., & Soker, N. 2011, MNRAS, 417, 1466
Kerzendorf, W. E., Childress, M., Scharwächter, J., Do, T., & Schmidt, B. P. 2014, ApJ, 782, 27
Koo, B.-C., Raymond, J. C., & Kim, H.-J. 2016, JKAS, 49, 109
Levanon, N., & Soker, N. 2019, ApJL, 872, L7
Levanon, N., Soker, N., & García-Berro, E. 2015, MNRAS, 447, 2803
Lewis, K. T., Burrows, D. N., Hughes, J. P., et al. 2003, ApJ, 582, 770
Li, C.-J., Chu, Y.-H., Gruendl, R. A., et al. 2017, ApJ, 836, 85
Li, C.-J., Kerzendorf, W. E., Chu, Y.-H., et al. 2019, ApJ, 886, 99
Liu, D., Wang, B., & Han, Z. 2018, MNRAS, 473, 5352
Livio, M., & Mazzali, P. 2018, PhR, 736, 1
Livio, M., & Riess, A. G. 2003, ApJL, 594, L93
Lopez, L. A., Ramirez-Ruiz, E., Huppenkothen, D., Badenes, C., & Pooley, D. A. 2011, ApJ, 732, 114
Marietta, E., Burrows, A., & Fryxell, B. 2000, ApJS, 128, 615
Meng, X., & Li, J. 2019, MNRAS, 482, 5651
Meng, X., & Podsiadlowski, P. 2017, MNRAS, 469, 4763
Meng, X., & Yang, W. 2010, ApJ, 710, 1310
Millard, M. J., Bhalerao, J., Park, S., et al. 2020, ApJ, 893, 98
Nomoto, K. 1982a, ApJ, 253, 798
Nomoto, K. 1982b, ApJ, 257, 780
Nomoto, K., & Leung, S.-C. 2018, SSRv, 214, 67
Ossenkopf, V., Henning, T., & Mathis, J. S. 1992, A&A, 261, 567
Ott, T. 2012, QFitsView: FITS file viewer, Astrophysics Source Code Library, ascl:1210.019
Raymond, J. C. 1979, ApJS, 39, 1
Raymond, J. C., Chilingarian, I. V., Blair, W. P., et al. 2020, ApJ, 894, 108
Rest, A., Suntzeff, N. B., Olsen, K., et al. 2005, Natur, 438, 1132
Reynolds, S. P., Borkowski, K. J., Hwang, U., et al. 2007, ApJL, 668, L135
Rolleston, W. R. J., Smartt, S. J., Dufton, P. L., & Ryans, R. S. I. 2000, A&A, 363, 537
Rudolph, A. L., Fich, M., Bell, G. R., et al. 2006, ApJS, 162, 346
Ruiz-Lapuente, P. 2019, NewAR, 85, 101523
Ruiz-Lapuente, P., Damiani, F., Bedin, L., et al. 2018, ApJ, 862, 124
Sankrit, R., Blair, W. P., Frattare, L. M., et al. 2008, AJ, 135, 538
Sankrit, R., Raymond, J. C., Blair, W. P., et al. 2016, ApJ, 817, 36
Sano, H., Yamane, Y., Tokuda, K., et al. 2018, ApJ, 867, 7
Seitenzahl, I. R., Ghavamian, P., Laming, J. M., & Vogt, F. P. A. 2019, PhRvL, 123, 041101
Shen, K. J., & Schwab, J. 2017, ApJ, 834, 180
Sutherland, R. S., & Dopita, M. A. 1993, ApJS, 88, 253
Totani, T., Morokuma, T., Oda, T., Doi, M., & Yasuda, N. 2008, PASJ, 60, 1327
Vancura, O., Blair, W. P., Long, K. S., & Raymond, J. C. 1992, ApJ, 394, 158
Wang, B., & Han, Z. 2012, NewAR, 56, 122
Wang, B., Zhou, W. H., Zuo, Z. Y., et al. 2017, MNRAS, 464, 3965
Wareing, C. J., Zijlstra, A. A., & O'Brien, T. J. 2007, MNRAS, 382, 1233
Webbink, R. F. 1984, ApJ, 277, 355
Whelan, J., & Iben, I., Jr. 1973, ApJ, 186, 1007
Williams, B. J., Blair, W. P., Blondin, J. M., et al. 2011, ApJ, 741, 96
Williams, B. J., Blair, W. P., Borkowski, K. J., et al. 2018, ApJL, 865, L13
Williams, B. J., Borkowski, K. J., Reynolds, S. P., et al. 2012, ApJ, 755, 3
Williams, B. J., Borkowski, K. J., Reynolds, S. P., et al. 2014, ApJ, 790, 139
Yamaguchi, H., Badenes, C., Petre, R., et al. 2014, ApJL, 785, L27